Nanoscale topological defects and improper ferroelectric domains in multiferroic barium hexaferrite nanocrystals

D. Karpov, Z. Liu, A. Kumar, B. Kiefer, R. Harder, T. Lookman, and E. Fohtung

Title: Nanoscale topological defects and improper ferroelectric domains in multiferroic barium-hexaferrite nanocrystals

Authors: D. Karpov[1][§], Z. Liu[2], A. Kumar[2], B. Kiefer[1], R. Harder[3], T. Lookman, and E. Fohtung[1,2]*

Affiliations:

[1]Department of Physics, New Mexico State University, Las Cruces, NM 88003, USA.

[2]Los Alamos National Laboratory, Los Alamos, NM 87545, USA.

[3]Advanced Photon Source, Argonne National Laboratory, Argonne, IL 60439, USA.

[§]Present address: Paul Scherrer Institute, Swiss Light Source, 5232 PSI-Villigen, Switzerland.

Corresponding authors: *efohtung@nmsu.edu

Abstract: Multiferroic materials that demonstrate magnetically driven ferroelectricity have fascinating properties such as magnetic (electric) field-controlled ferroelectric (magnetic) response that can be used in transformative applications including fast-writing, power-saving, and nondestructive data storage technologies in next-generation computing devices. However, since multiferroicity is typically observed at low temperatures, it is highly desirable to design multiferroic materials that can operate at room temperature. Here we show that $BaFe_{12}O_{19}$ is a promising room-temperature multiferroic material, and we unravel in 3D the dynamics of topological defects, strain and improper ferroelectric domains driven by electric fields in individual $BaFe_{12}O_{19}$ nanocrystals. Using Bragg Coherent Diffractive Imaging in combination with group-theoretical analysis, first-principles density functional calculations of phonons and Landau phase-field theory we uncover in 3D the dynamics of topological defects, strain and improper ferroelectric domains driven by electric fields in individual $BaFe_{12}O_{19}$ nanocrystals. Our results show that $BaFe_{12}O_{19}$ is an improper ferroelectric, in contrast to the current paradigm that adheres to the absence of improper ferroelectricity. Moreover, the fine structure of the reconstructed Bragg electron density suggests that $BaFe_{12}O_{19}$ may be able to harbor novel topological quantum states of matter and a pathway to transform information technologies.

Main Text: Topological defects are ubiquitous in condensed matter physics where their role in symmetry-breaking phase transitions is currently a prime topic in high-temperature superconductivity[1-5], multiferroics[6-8], liquid crystals[9, 10], [3]He and [4]He superfluids[11-14]. In multiferroics, physical properties of topological defects, such as coupling between structural, charge, and spin degrees of freedom, are different from the bulk properties of the parent material. This exotic property together with the possibility of controlled writing of topological defects can lead to breakthrough applications in novel electronics, energy storage, and new forms of matter.

For a long time, studies of topological defects in cosmology are limited to numerical simulations due to the impracticality of cosmological scale experiments and an absence of alternatives. Recently multiferroic hexagonal manganites ($RMnO_3$, R=Sc, Y, In, Dy-Lu) have been actively studied as a system where topological defects may behave according to Kibble-Zurek

scaling law[6-8], resulting in three-dimensional imaging of vortex loops condensation through use of electron microscopy and surface polishing tools[7]. However, in spite of significant progress both in experimental observations and theoretical modeling there has been a lack of coherent understanding of the observed phenomena[15]. One limitation is the absence of systems different from hexagonal manganites but with similar topological behavior. The other limitation is the inability of electron imaging techniques to be used for whole-volume time-dependent studies under external stimuli.

M-type hexaferrites such as barium hexaferrite $BaFe_{12}O_{19}$ (BHF) have attracted attention because of their excellent magnetic properties and potential applications. BHF is a widely used ferrite permanent magnet with a magnetization per formula unit at T=0 K of M=20 μB[16]. The crystal structure of BHF consists of alternating octahedral, tetrahedral and bipyramidal S, R, $S*$ and $R*$ blocks (**Figure 1A**) with the asterisk symbols denoting the corresponding blocks that are rotated by 180° about the c-axis. In work[17] BHF was investigated as a quantum paraelectric with a Tc of 6K. Other studies suggests large spontaneous polarization in bulk BHF ceramics at room temperature[18, 19] with a maximum remnant polarization of 11.8 $\mu C/cm^2$ [18]. It thus holds promise as a low toxicity, lead-free multiferroic. However, it is well-known that for ferroelectricity to coexist with magnetism, the nature of the ferroelectricity cannot be that found in prototypical perovskite ferroelectrics such as $PbTiO_3$[20]. Traditional prototype systems such as hexagonal manganites form a class of multiferroic materials that are simultaneously ferroelectric and antiferromagnetic[21]. In these prototypical "geometric ferroelectric" systems, first-principles calculations have shown that the usual indicators of ferroelectric instability (e.g. large Born effective charges) are absent. For example, in $YMnO_3$ the spontaneous polarization of $6\mu C/cm^2$ results from the tilting of the Mn-centered oxygen octahedra and buckling of the Y-O planes, with no significant off-centering of the Mn cations[21], suggesting a phonon-mediated contribution to ferroelectricity.

Here we use X-ray Bragg coherent diffractive imaging (BCDI)[22, 23] to reconstruct 3D strain maps of BHF nanoparticles and gain an understanding of unusual properties of this material. The theory is consistent with these observations and provides additional insights into the origin of improper ferroelectricity in this system. Our observations show ferroelectric $\mathbf{Z_2 x Z_3}$ vortex loops spanning the volume of nanoparticles suggesting the use of BHF as an alternative to rare-earth manganites for studies of Kibble-Zurek mechanism in condensed matter. By applying low voltage electric fields, we are enabled to study the dynamics of ferroelectric vortex loops and the vorticity (Chern/winding number) of ferroelectric polarization near the loops. These loops appear to be stable and locally pinned due to the topologically protected ferroelectric vortices. With the aid of Landau theory, we identify six antiphase ferroelectric domains with up/down polarization configurations that form a vortex or an antivortex (see Appendix B). Our results suggest that the observed ferroelectric vortex loops belong to the same universality class as cosmological strings.

Results

To perform BCDI experiment, BHF nanoparticles were first synthesized by a polymer precursor method, pressed into pellets, sintered into ceramics, and enclosed in the functional capacitor (see Appendix C, D, E, and Figure S1). The functional capacitor allows electric field application on individual BHF nanoparticles. Random orientation of the nanoparticles allows the diffraction peaks to be isolated in our BCDI experiment. During the experiment, we distinguished nanoparticles undergoing structural phase transitions by tracking their characteristic asymmetrical diffraction patterns[23]. These coherent diffraction patterns are measured and recorded near the (107) Bragg peak. To record the 3D diffraction data (see Figure S2), we rocked the isolated nanocrystal with respect to the incident x-ray beam. Iterative phase retrieval algorithms are used to invert the

diffraction into 3D real space images that confirm a model predicted by Landau theory. Three-dimensional real-space images of a BHF nanoparticle were reconstructed with approximately 15 nm spatial resolution determined by the phase retrieval transfer function (see Figure S3). For more information on the experimental and reconstruction procedures please see Appendix F and G. We illustrate the capabilities of BCDI by visualizing an isosurface (Figure 2A) of the reconstructed magnitude of the 3D Bragg electron density of BHF to show the shape and size of the nanoparticle. The physical density of the crystal at the nanoparticle surface is almost constant with no defects (colored isosurface in Figure 2A) but there is a prominent region within the nanoparticle (Figure 2B) with non-constant density, that can be associated with the presence of topological defects[23]. In this prominent region, the imaginary part of the complex Bragg electron density shows features originating from an internal displacement field as shown in Figure 2B-D. The maximum phase shift of the complex density of 1.55 radians corresponds to a total displacement (relative to the ideal crystal lattice) of about 0.14 nm for BHF {107} atomic spacing (see Figure 2). We identify and classify two types (see Figure 2C) of vortex condensate pairs: type-I (antivortex-vortex) and type-II (antivortex-antivortex). The vortex phase condensate pairs are connected by strings (vortex lines) visualized on Figure 3A.

To illuminate the origin of ferroelectric displacement pattern we used Landau phase-field model[24] of improper ferroelectricity for spatially uniform states of hexagonal manganites that was extended by a symmetry breaking E·P term to account for an applied external electric field. Under applied 10 V (see Figure 3C-D) we notice changes in the morphology of the ferroelectric BHF nanoparticle as compared to the morphology at 0 V (see Figure 3A-B). However, anti-phase domains do not change their relative order (see Figure 3E-F), which indicates that ferroelectric vortices do not switch and are topologically protected for the given applied voltage (behavior identical to hexagonal manganites). The width of each anti-phase domain oriented anti-parallel to the direction of electric field application is reduced by the field. We associate this behavior with the topologically protected vortex loops observed in Figure 3 as the integrity of the vortex core is preserved along the string length.

Analysis of the symmetry character of phonon eigenvectors of relaxed structures (see Appendix A) for ferromagnetic and antiferrimagnetic orderings in the paraelectric P63/mmc (#194) structure shows that a change in magnetic ordering from ferromagnetic to antiferrimagnetic induces a displacement pattern which couples with the K1 mode and lowers the crystal symmetry. Allowing full relaxation of the P63/mmc (#194) structure with antiferrimagnetic ordering, we find that it finally relaxes to P63/mcm (#193), an intermediate paraelectric structure. The relaxed P63/mcm structure is energetically lower compared to the parent P63/mmc structure by ~20 meV/f.u. The energy of the ferroelectric P63cm (#185) structure is almost the same as the paraelectric structure P63/mcm. Thus, unlike $YMnO_3$, where the K3 mode drives the improper ferroelectricity, here we find that it is the K1 mode that couples with the antiferrimagnetic spin ordering and drives the improper ferroelectricity in BHF. K1 and the polar mode Γ_2^- together will drive the parent to the ferroelectric phase. Our results show that the two-phonon modes are almost degenerate, hindering the detailed identification of the transition path since all linear combinations of the two degenerate eigen displacement vectors cannot be distinguished, at least in the harmonic approximation. Using berry phase calculations in the P63cm we estimate polarization 2.5 $\mu C/cm^2$ along z direction. Thus, improper ferroelectricity is an important contribution to the electrical polarization in BHF.

Next, we investigate whether multiferroic BHF undergoes symmetry lowering transitions analogous to that in the early Universe, making it a candidate system for studies of topological defects of the same universality class as cosmic strings. Our first-principles calculations (see

Appendix A) and existing studies of $YMnO_3$[6-8, 15, 21, 24], suggest a structural phase transition above 1600 K resulting in a periodic lattice distortion (Figure 1B-C) with a potential energy landscape similar to the one of the early Universe (Figure 1D). A consequence of this unusual potential landscape is the structure with six anti-phase domains (α^+, β^-, γ^+, α^-, β^+, γ^-) with opposite electric polarization (Figure 1C) resulting in the formation of a topologically protected $\mathbf{Z_2 \times Z_3}$ vortex[25, 26].

The consistent observation of clover-leaf domain patterns in the reconstructed ferroelectric displacement maps and modelled in Landau phase-field simulations, as well as the origin of improper ferroelectricity, suggest that imaged topological strings are indeed analogous to those reported in hexagonal manganites and they share the same universality class with cosmic strings. By mapping the vorticity of the ferroelectric polarization (Figure 4), we observe that the vorticity is geometrically constrained near the vortex cores. Along the length of the loops, the vorticity accumulates an extra phase of $7\pi/4$ (Figure 4B) and $3\pi/4$ (Figure 4D) when the nanoparticle is under 0V and 10V, respectively. Since the phase difference is π, the quantum mechanical wave function representing the vorticity can be thought of as 2D quasi-particles whose wave function changes sign under an applied electric field of 10 V and could potentially obey Fermi, Bose-Einstein statistics or even non-Abelian braid statistics that describes the thermodynamics of 2D anyon quasiparticles and breaking the low-temperature tyranny of quantum effects.

Discussion

Multiferroic nanocrystals can be driven far from equilibrium by external perturbations such as heat, light, electric and magnetic fields. Four primary ferroic orders namely toroidal, dipole, elastic and magnetic moments can be tuned at the microscopic level and used in the design of novel devices. For instance, ferroelectric domain walls, vortices, and other topological defects are promising as active components in transformative nanoelectronics[24] since they can carry properties which do not occur in the bulk and their position and vorticity can actively be controlled by external perturbations. BCDI is a suitable tool to probe such order parameters. In our work, we focus on BHF and show through first-principles electronic calculations combined with group theoretical analysis, a mechanism of improper ferroelectricity in this system. Performing BCDI experiment and consecutive Landau phase-field modelling we observe multiple topological loops in the volume of a 500 nm nanoparticle.

Previous studies of vortex loops in hard condensed matter were limited to non-destructive imaging of surface phenomena[6, 8, 15] or destructive imaging of the volume through combination of electron microscopy and polishing techniques[7]. By utilizing coherent X-rays we were able to simultaneously access the 3D information on and demonstrate that this can be combined with external influences (application of electric fields for the case of current study, but not limited to that).

Our work opens avenues for in-operando 3D imaging of topological defect dynamics and studies of order parameter changes induced by external perturbations in functional nanodevices. We demonstrate that topological defects analogous to cosmic strings, hypothesized to emerge after the Big Bang, can be studied non-destructively by BCDI in multiferroic BHF under applied external perturbations. In future experiments, THz sources at x-ray free-electron laser facilities can assist in driving this material along a selected phonon mode identifying the predicted symmetry change to expand our study into the ultrafast domain. Our results suggest that coherent X-ray diffraction studies of multiferroics could serve to shed light on mysteries of the universe while geometric constraints to the Bragg electronic density and vorticity degrees of freedom can generate novel topological room temperature quantum states of matter.

APPENDIX A: DENSITY FUNCTIONAL THEORY

To understand the energetics of different magnetic orderings and ferroelectric distortions in barium hexaferrite $BaFe_{12}O_{19}$ (BHF), we performed density functional theory (DFT) calculations using generalized gradient approximation (GGA) for the exchange-correlation functional with the Perdew-Becke-Erzenhof (PBE) parametrization[27] as implemented in the VASP package[28,29]. The interaction between the valence electrons and ionic cores is treated using PAW potential[30]. We used a plane wave energy cutoff of 500 eV and optimized the atomic structure until the force on each atom is smaller than 0.01 eV/A. We used 9x9x3 and 5x5x3 Gamma-centered Monkhorst Pack[31] k-point mesh to integrate the Brillouin Zones for 64 and 192 atom unit cells (corresponding to Z=2 and Z=6) respectively.

To identify the ground state magnetic ordering in BHF, we calculated the energetics for ferromagnetic ordering (all spins up), antiferromagnetic ordering (Fe1, Fe2, Fe3, Fe4 spins are up and Fe5 spins are down), and antiferrimagnetic ordering (Fe1, Fe2, Fe5 are up and Fe3, Fe4 spins are down) and found that the antiferrimagnetic ordering has the lowest energy. This is consistent with experimental observations and earlier studies. Energetically, the relaxed structure (P63/mmc #194) for antiferromagnetic and antiferrimagnetic orderings are lower compared to ferromagnetic ordering by 2.89 eV/f.u. and 3.85eV/f.u. respectively. The calculated magnetic moments for ferromagnetic and antiferrimagnetic are 59 μ_B/f.u. and 19.5 μ_B/f.u., respectively. Parameters of the relaxed crystal structure for BHF (Z=2) with the antiferrimagnetic ordering is provided in Table S1 in Ref. [32].

Next, we calculated the phonons at q=0 for the antiferrimagnetic ordering (Z=2) in P63/mmc structure and found that all phonon modes are stable. The phonon frequency for the Γ_2^- is 68 cm^{-1}. This is consistent with the observation of improper ferroelectricity in hexagonal manganite $YMnO_3$[21], where Γ_2^- mode is stable but zone boundary mode K3 is unstable. Ferroelectricity in $YMnO_3$ is driven by coupling between Γ_2^- and K3 mode[21]. To find whether the zone boundary modes are unstable in BHF, we performed phonon calculations at q=0 in tripled supercell (consisting of 192 atoms, Z=6) but again found that all phonon modes are stable and that means that zone boundary mode K3 is stable in BHF unlike it is in $YMnO_3$. To confirm it, we also calculated the energy as a function of mode displacement for three modes Γ_2^-, K1, and K3 (see Figure S11) and it shows that all three modes are stable. We thus suggest structural path that favors ferroelectricity in BHF as shown on Figure S12.

APPENDIX B: LANDAU THEORY

To interpret our BCDI results, we adopt the Landau theory [24] of improper ferroelectricity for spatially uniform states of hexagonal manganites and include an explicit symmetry breaking term $\boldsymbol{E} \cdot \boldsymbol{P}$ that accounts for the external electric field. The free-energy expansion in powers of the amplitude of the trimerization Q, polarization P, and phase Φ is given by:

$$F = \frac{a}{2}Q^2 + \frac{b}{4}Q^4 + \frac{Q^6}{6}Q^6(c + c'\cos6\Phi) - gQ^3P\cos3\Phi + \frac{a_P}{2}P^2 - EP, \qquad (1)$$

where a, b, c, c', g, and a_P are parameters of the phenomenological expansion of the free energy equation obtainable from *ab initio* calculations (see Table S2 in Ref. [32]). The simulated trimerization phase Φ (see Figure S9c) and the amplitude Q (see Figure S9a), play an important role in the theory of topological defects and 1D string behavior. In particular, the form of the nonlinear coupling arising from the equilibrium condition ($\partial F/\partial P$=0) giving rise to improper ferroelectric polarization:

$$P = gQ^3\cos3\Phi - E, \qquad (2)$$

which is emphasized within the nanoparticle shown in Figure S9b. We use these simulations to interpret BCDI reconstructions of topological defects, ferroelectric domains and 1D strings. In our studies, the locations of vortices manifest themselves as regions in the amplitude map (see Figure 2, 3, 4, and S8), around which Φ changes monotonically in a clockwise (α^+, γ^-, β^+, α^-, γ^+, β^-) or counterclockwise (α^+, β^-, γ^+, α^-, β^+, γ^-) fashion as shown. Equation 2 indicates that under an external electric field the structural phase transition can affect the nature and symmetry of the Mexican hat-type potential (see Figure S10). At zero electric fields the Mexican hat potential has six minima in the brim that correspond to alternating polarization directions (α^+, γ^-, β^+, α^-, γ^+, β^-).

To understand the arrangement of ferroelectric phases in the experimental reconstructions we used the reconstructed polarization maps and the particle shape as initial conditions for the phase field modelling. This allowed to separate different phases (α, β, γ) in BCDI reconstructions that comply with physically realistic conditions.

APPENDIX C: SAMPLE PREPARATION
By employing a polymer precursor method, barium hexaferrite $BaFe_{12}O_{19}$ nanopowders were prepared from barium acetate $(CH_3COO)_2Ba$ and ferric acetylacetonate as the starting ingredients. Typically, we dissolved about 0.258 g of barium acetate in 15 mL distilled water to form a clear solution which is later stored in a three-neck glass bottle. To avoid the hydrolysis of ferric acetylacetonate these procedures were conducted in a glove box. Later, 3.7082 g ferric acetylacetonate was dissolved in 200 mL of benzene.

Prepared barium acetate solution and the ferric acetylacetonate in benzene, under the stoichiometric atomic ratio of Ba/Fe=1/10.5 was continuously heated and stirred for 1 hour to create a homogenous mixture of both solutions at an approximate temperature of 303.15 K. Then a 15 ml polyethylene glycol mixture solution and 100 ml ammonia were added into the above solution to form a colloid dispersion solution. The dispersion solution was kept at 323 K while stirring for 8 hours and the colloid solution was then taken out of the glove box.

We used centrifugation methods to remove the organic products and water. Leftover colloidal powders were calcined at 724 K for 1.5 h to remove remaining organic components. Three different parts of 0.15 g nanopowder were pressed into pellet crystals, which were then placed in individual Pt crucible and heated to 1600 K for 24 hours in air. Finally, pellets were quenched to room temperature at a rate of 275K per minute. X-ray laboratory powder diffraction (see Figure S4) and scanning electron microscopy (see Figure S5) confirmed the random orientation of facets in the prepared sample, which is necessary to record isolated peaks from nanoparticles in the BCDI technique[22, 23].

APPENDIX D: FUNCTIONAL CAPACITOR AND ELECTRIC FIELD CONTROL
To perform the application of an external electric field to pellets of BHF, we prepared a functional capacitor as shown in Figure S1. The pellet of BHF with dimensions 0.5 x 2 x 2 mm3 was immersed in non-polarizing polymer based on bisphenol-A-epoxy[23]. The top and bottom sides of the prepared matrix were covered with a composite made of the same polymer with dispersed conducting carbon nanoparticles (70% by volume) to form two conducting surfaces. The mixture was then cured with a commercially available agent in an oven for 3 hours at 95 ºC. Gold electrodes were later sputtered on two diagonally opposite edges providing outlets for wire bonding of the functional capacitor.

To apply an electric field in a controlled and programmable manner, we used a Precision Premier II Ferroelectric Tester. The system allows in-situ feedback monitoring of the sample's ferroelectric response and waveform application through an arbitrary waveform generator with pulse

widths down to 0.5 µs. The system can monitor global hysteresis, leakage, induced charge, resistivity and other properties during the experiment with maximum charge and voltage resolution of 0.8 fC and 76 µV respectively.

APPENDIX E: MULTIFERROIC PROPERTIES OF BARIUM HEXAFERRITE

The measurements of ferroelectric response (see Figure S6a) was done using Precision Premier II Ferroelectric Tester manufactured by Radiant Technologies, same system that was used during the experiment at synchrotron for applying and monitoring driving voltage. One can see strong leakage in the ferroelectric response that is due to the construction of ferroelectric capacitor where we have conducting carbon particles in polymer matrix. We presume that in certain areas the particles create conducting chains, enough to degrade global performance of the capacitor but not enough to short-circuit two plates. Measurements of ferromagnetic properties are very challenging on the powder systems and thus were performed on separately grown thin films (see Figure S6b).

APPENDIX F: EXPERIMENTAL PROCEDURE

A Si (111) monochromator sector 34-ID-C of Advanced Photon Source was used to select coherent X-ray photons with an energy of 9.0 keV. The beam had an energy bandwidth of 1eV defining the monochromaticity and 0.7 µm transverse coherence length. Focusing of the X-rays onto the sample was done by a pair of Kirkpatrick-Baez mirrors set after the beam defining aperture. Beam size for this experiment was 700 nm by 700 nm.

A schematic showing the principle of Bragg coherent diffraction experiment is depicted in Figure S7. A motorized arm allowed to position the location of a Medipix2 CMOS X-ray detector around the diffraction sphere. We align the detector position to the outgoing (107) characteristic Bragg reflection from the BHF sample.

The detector was positioned at a distance of 1.2 m from the sample to zoom into the interference fringes in the diffraction pattern. An evacuated flight tube placed in the sample-to-detector path helps to decrease the loss of photons scattered in the air. The use of an evacuated flight tube, high sensor gain, as well as photon counting mode of the detector, are crucial for such photon-starving technique as nanoscale Bragg coherent diffractive imaging.

The rocking curve was collected as a series of 2D diffraction patterns in the vicinity of the BHF {107} Bragg peak corresponding to $2\theta = 28.5°$ with the scanning range of $\Delta\theta = \pm0.24°$ about the Bragg peak origin. Throughout a single rocking curve, a total scan of 100 patterns was collected. The dataset for the virgin state E_1 was collected before cycling the functional capacitor. The following state under applied electric field E_2 was recorded after 30 cycles of applied and released electric field. This allowed us to make sure that the system underwent a phase-transition under applied electric field.

APPENDIX G: RECONSTRUCTION PROCEDURE

The recorded 3D diffraction patterns (see Figure S2) in reciprocal space is then inverted into a direct space 3D image of the nanoparticle after the phase Φ and amplitude Q of the complex wave-field $\rho(r) = Q(r)e^{i\Phi(r)}$ are iteratively retrieved[22,23,33]. The reconstructed phases Φ scale linearly with the displacement field $\mathbf{u}_{107}$ for a given reciprocal lattice vector $\mathbf{G}_{107}$ according to the relationship $\Phi(\mathbf{r})=\mathbf{G}_{107}\cdot\mathbf{u}_{107}$. The shape and size of the nanoparticle can be estimated from the isosurface of reconstructed Bragg electron density (see Figure 2A). For a given external electric field, real-space images of the BHF nanoparticles were reconstructed with approximately 15 nm spatial resolution as determined by the phase retrieval transfer function (see Figure S3). The

reconstruction allows us to conveniently slice through the volume of the nanoparticle at a given external electric field and analyze signatures of topological defects (Figure 2B-D).

Iterative phase retrieval algorithms based on Fienup's Hybrid Input-Output (HIO) method with additional randomized over-relaxation (O_R) were utilized[34]. Inverting the diffraction data is a critical step that uses a computer algorithm that takes advantage of internal redundancies when the measurement points are spaced close enough together to meet the oversampling requirement[35]. The first step is to postulate a 3D support volume in which all the sample density will be constrained to exist. These methods impose a backward and forward Fourier transform between the reciprocal space and the real-space, with the support constraint imposed in the latter and an intensity mask constraint in the former[36].

The iterative scheme of ($HIO+O_R$) + ER algorithm used in the current work is shown in Figure S8. The main difference between conventional HIO and the HIO with randomized over-relations is that in the later algorithm a projection operator is replaced by:

$$Q_{A;\lambda_A} = 1 + \lambda_A(\mathbf{P}_A - 1), \tag{3}$$

with λ_A as a relaxation parameter[34] which is randomized in the range of [0.5, 1.5] for each iteration. This operation holds for the reconstruction part in the reciprocal space while the real space part is identical to conventional HIO. Major improvement of the algorithm against the stagnation problem is the fact that due to randomization of relaxation parameter the 'stagnation space' also alters at each iteration while the solution space is unique and does not depend on the value or dynamic of the relaxation parameter, insuring significant success rates[34].

A total of 7600 iterations consisting of N_{ER} = 20 and N_{HIO+OR} = 380 were performed on the measured 3D coherent diffraction data when the BHF nanoparticle was subjected to 0V and 10V respectively. The reconstructed 3D phases were unwrapped to obtain the ferroelectric displacement fields (at 0V and 10V). The phase reconstructions were then projected on single isosurface contoured at a given maximum density.

To confirm the reproducibility and uniqueness of the obtained solutions, we performed a series of phase retrieval procedures with different random input phases for the measured scattered radiation. We define a measure for the error in the following form[34]:

$$\epsilon^{(i)} = \frac{\sum_{\mathbf{q}}(|F_{sim}^{(i)}(\mathbf{q})| - I_{\exp}(\mathbf{q}))^2}{\|I_{\exp}\|_2^2} \tag{4}$$

where $F_{sim}^{(i)}(\mathbf{q})$ is the magnitude of the reconstructed amplitude and $I_{\exp}(\mathbf{q})$ is the experimental intensity in the reciprocal space. An estimate of the resolution of the resulting reconstruction was obtained using the Phase Retrieval Transfer Function (PRTF) [37, 38]:

$$PRTF(\mathbf{q}) = \left\langle \left| \frac{|F_{sim}(\mathbf{q})|\exp{(i\varphi_{sim}(\mathbf{q}))}}{\||F_{sim}(\mathbf{q})|\exp{(i\varphi_{sim}(\mathbf{q}))}\|} \right| \right\rangle$$

The PRTF allows to analyze correlations in reconstructed phases over a number of converged solutions. The less correlated the phases are, the lower is the value of PRTF. In the analysis, the PRTF is weighted for a given spatial frequency, with conventional threshold being set at 50% of PRTF for the frequencies that are reconstructed with reproducible phases[37]. For our results, we achieved 15 nm spatial resolution (see Figure S3).

References:

[1]   S. R. Shenoy, B. Chattopadhyay, Anisotropic three-dimensional XY model and vortex-loop scaling. Phys. Rev. B 51, 9129–9147 (1995).

[2]   D. Domínguez, N. Grønbech-Jensen, A. R. Bishop, S. R. Shenoy, Transformer configuration in three dimensional Josephson lattices at zero magnetic field. Phys. Rev. Lett. 75, 717–720 (1995).

[3]   M. Kiometzis, H. Kleinert, A. M. J. Schakel, Critical exponents of the superconducting phase transition. Phys. Rev. Lett. 73, 1975–1977 (1994).

[4]   A. K. Nguyen, A. Sudbø, Onsager loop transition and first-order flux-line lattice melting in high-Tc superconductors. Phys. Rev. B 57, 3123–3143 (1998).

[5]   F. Wilzcek, Fractional Statistics and Anyon Superconductivity (World Scientific, 1990).

[6]   S. M. Griffin, M. Lilienblum, K. T. Delaney, Y. Kumagai, M. Fiebig, N. A. Spaldin, Scaling Behavior and Beyond Equilibrium in the Hexagonal Manganites. Phys. Rev. X 2, 041022 (2012).

[7]   S.-Z. Lin, X. Wang, Y. Kamiya, G.-W. Chern, F. Fan, D. Fan, B. Casas, Y. Liu, V. Kiryukhin, W. H. Zurek, C. D. Batista, S.-W. Cheong, Topological defects as relics of emergent continuous symmetry and Higgs condensation of disorder in ferroelectrics. Nature Physics 10, 970–977 (2014).

[8]   Q. N. Meier, M. Lilienblum, S. M. Griffin, K. Conder, E. Pomjakushina, Z. Yan, E. Bourret, D. Meier, F. Lichtenberg, E. K. H. Salje, N. A. Spaldin, M. Fiebig, A. Cano, Global formation of topological defects in the multiferroic hexagonal manganites. Phys. Rev. X. 2017, 7, 041014.

[9]   I. Chuang, B. Yurke, R. Durrer, N. Turok, Cosmology in the laboratory - Defect dynamics in liquid crystals. Science 251, 1336–1342 (1991).

[10]   S. Ducci, P. L. Ramazza, W. González-Viñas, F. Arecchi, Order parameter fragmentation after a symmetry breaking transition. Phys. Rev. Lett. 83, 5210 (1999).

[11]   P. Hendry, N. Lawson, R. Lee, P. V. McClintock, C. Williams, Generation of defects in superfluid 4He as an analogue of the formation of cosmic strings. Nature 368, 315 (1994).

[12]   M. E. Dodd, P. Hendry, N. Lawson, P. V. McClintock, C. Williams, Nonappearance of vortices in fast mechanical expansions of liquid 4He through the lambda transition. Phys. Rev. Lett. 81, 3703-3706 (1998).

[13]   V. M. H. Ruutu, V. B. Eltsov, A. J. Gill, T. W. B. Kibble, M. Krusius, Yu. G. Makhlin, B. Plaçais, G. E. Volovik, W. Xu, Vortex formation in neutron-irradiated superfluid 3He as an analogue of cosmological defect formation. Nature 382, 334-336 (1996).

[14]   C. Bäuerle, Y. M. Bunkov, S. Fisher, H. Godfrin, G. Pickett, Laboratory simulation of cosmic string formation in the early universe using superfluid 3He. Nature 382, 332–334 (1996).

[15]   M. E. Holtz, K. Shapovalov, J. A. Mundy, C. S. Chang, Z. Yan, E. Bourret, D. A. Muller, D. Meier, and A. Cano, Topological Defects in Hexagonal Manganites: Inner Structure and Emergent Electrostatics. Nano Lett. 17, 5883-5890 (2017).

[16]   B. D. Cullity and C. D. Graham, Introduction to Magnetic Materials (2nd edition, Wiley 2009).

[17]   S. E. Rowley, Y.-S. Chai, S.-P. Shen, Y. Sun, A. T. Jones, B. E. Watts, J. F. Scott, Uniaxial ferroelectric quantum criticality in multiferroic hexaferrites BaFe12O19 and SrFe12O19. Scientific Reports 6, 25724 (2016).

[18]   G. Tan, X. Chen, Structure and multiferroic properties of barium hexaferrite ceramics. J. of Magn. and Magn. Mat. 327, 87-90 (2013).

[19]   V.G. Kostishyn, L.V. Panina, A.V. Timofeev, L.V. Kozhitov, A.N. Kovalev, A.K. Zyuzin, Dual ferroic properties of hexagonal ferrite ceramics BaFe12O19 and SrFe12O19. J. of Magn. and Magn. Mater. 400, 327–332 (2016).

[20]   N. A. Hill, Why Are There so Few Magnetic Ferroelectrics? J. Phys. Chem. B. 104, 6694–6709 (2000).

[21]   C. J. Fennie, K. M. Rabe, Ferroelectric transition in YMnO3 from first principles. Phys. Rev. B 72, 100103(R) (2005).

[22]   A. Ulvestad, A. Singer, J. N. Clark, H. M. Cho, J. W. Kim, R. Harder, J. Maser, Y. S. Meng, O. G. Shpyrko, Topological defect dynamics in operando battery nanoparticles. Science 348, 1344-1347 (2015).

[23]   D. Karpov, Z. Liu, T. d. S. Rolo, R. Harder, P.V. Balachandran, D. Xue, T. Lookman, E. Fohtung, Three-dimensional imaging of vortex structure in a ferroelectric nanoparticle driven by an electric field. Nature Communications 8, 280 (2017).

[24]   S. Artyukhin, K. T. Delaney, N. A. Spaldin, M. Mostovoy, Landau theory of topological defects in multiferroic hexagonal manganites. Nat. Mater. 13, 42-49 (2014).

[25]   Y. Kumagai, N. A. Spaldin, Structural domain walls in polar hexagonal manganites. Nature Communications 4, 1540 (2013).

[26]   Q. H. Zhang, L. J. Wang, X. K. Wei, R. C. Yu, L. Gu, A. Hirata, M. W. Chen, C. Q. Jin, Y. Yao, Y. G. Wang, X. F. Duan, Direct observation of interlocked domain walls in hexagonal RMnO3 (R=Tm, Lu). Phys. Rev. B. 85, 020102(R) (2012).

[27]   J. P. Perdew, K. Burke, M. Ernzerhof, Generalized gradient approximation made simple. Phys. Rev. Lett. 77, 3865–3868 (1996).

[28]   G. Kresse, J. Furthmuller, Efficiency of ab-initio total energy calculations for metals and semiconductors using a plane-wave basis set. Computational Materials Science 6, 15-50 (1996).

[29]   G. Kresse, J. Furthmuller, Efficient iterative schemes for ab initio total-energy calculations using a plane-wave basis set. Phys. Rev. B 54, 11169–11186 (1996).

[30]   P. E. Blochl, Projector augmented-wave method. Phys. Rev. B 50, 17953-17979 (1994).

[31]   H. J. Monkhorst, J. D. Pack, Special points for brillouin-zone integrations. Phys. Rev. B 13, 5188–5192 (1976).

[32]   See Supplemental Material at [URL will be inserted by publisher] for additional figures and tabulated values used in modelling.

[33]   I. Robinson, R. Harder, Coherent X-ray diffraction imaging of strain at the nanoscale. Nature Materials 8, 291-298 (2009).

[34]   M. Köhl, A. A. Minkevich, T. Baumbach, Improved success rate and stability for phase retrieval by including randomized overrelaxation in the hybrid input output algorithm. Optics Express 20, 17093-17106 (2012).

[35]   D. Sayre, Some implications of a theorem due to Shannon. Acta Cryst. 5, 843 (1952).

[36]   A. A. Minkevich, E. Fohtung, T. Slobodskyy, M. Riotte, D. Grigoriev, M. Schmidbauer, A. C. Irvine, V. Novák, V. Holý, T. Baumbach, Selective coherent x-ray diffractive imaging of displacement fields in (Ga,Mn)As/GaAs periodic wires. Phys. Rev. B 84, 054113 (2011).

[37]   H. N. Chapman, A. Barty, S. Marchesini, A. Noy, S. P. Hau-Riege, C. Cui, M. R. Howells, R. Rosen, H. He, J. C. H. Spence, U. Weierstall, T. Beetz, C. Jacobsen, D. Shapiro, High-resolution ab initio three-dimensional x-ray diffraction microscopy. J. Opt. Soc. Am. A. 23, 1179–1200 (2006).

[38]   S. Marchesini, H. N. Chapman, A. Barty, C. Cui, M. R. Howells, J. C. H. Spence, U. Weierstall, A. M. Minor, Phase aberrations in diffraction microscopy. IPAP Conf. Series 7, 380-382 (2006).

[39]   A. Kumar, C. J. Fennie, K. M. Rabe, Spin-lattice coupling and phonon dispersion of $CdCr_2O_4$ from first principles. Phys. Rev. B. 2012, 86.

[40]   J. Smit, H. P. J. Wijn, Ferrites: physical properties of ferrimagnetic oxides in relation to their technical applications (Eindhoven : N.V. Philips Gloeilampenfabrieken, 1959).

Author contributions: E.F. designed and conceived the project. E.F., D.K., and R.H performed the BCDI measurements and E.F. performed the phase retrieval analysis. A.K and T.L performed the group-theoretical analysis and first-principles density functional calculations. A.K, Z.L. B.K., and T.L. performed the phase field computation and theoretical interpretation. D.K. and E.F. characterized the $BaFe_{12}O_{19}$ nanoparticles and designed and assembled the sample. E.F. wrote the manuscript with contributions from all authors.

Competing interests

The authors declare no competing financial interests.
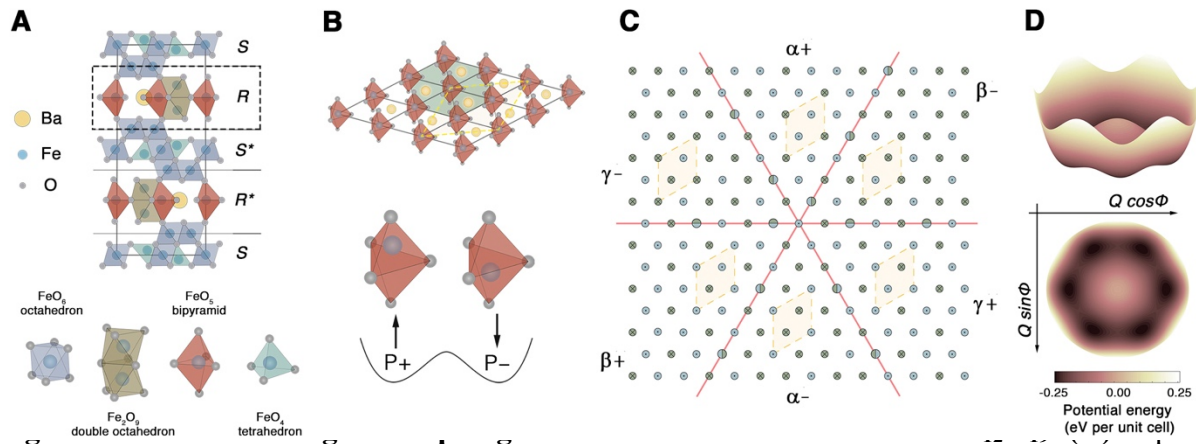
representation of the crystal structure of $BaFe_{12}O_{19}$. **(B)** A 2D triangular lattice of the FeO_5 bipyramids formed from R and $R*$ blocks. The off equatorial displacements of Fe^{3+} within the bipyramids generate an upwards ($P+$) and downwards ($P-$) electric polarization while the tilting of the FeO_5 trimerizes the unit cell to induce different orientated antiphase domains. **(C)** The corresponding atomic structures near a vortex core. **(D)** The Mexican-hat potential energy landscape of $BaFe_{12}O_{19}$. At higher energy (the peak of the hat) the energy is independent of the angle of trimerization, and the system has $U(1)$ symmetry. At lower energy (in the brim of the hat), six of the trimerization angles become favorable (dark circles), and the symmetry reduces to the six-fold discrete symmetry known as $\mathbf{Z_6}$.
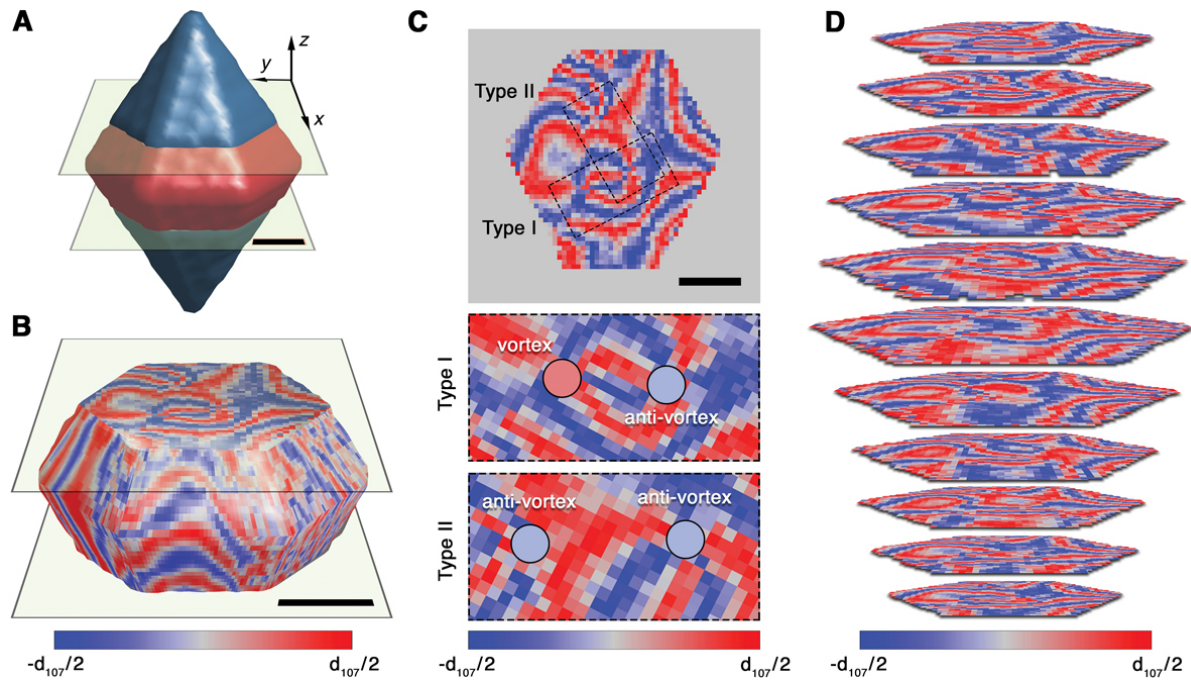
Figure 2. Three-dimensional spatial maps of $Z_2 \times Z_3$ domains and Z_6 vortices. (A) BCDI reconstructed $BaFe_{12}O_{19}$ nanoparticle shape with the transparent green planes denoting the locations at which a prominent volume of interest is extracted. **(B)** Projections of FE displacement field on an isosurface of the extracted volume-of-interest that hosts 1D strings. **(C)** Top slice of the volume-of-interest in **B**, showing domain pattern in $BaFe_{12}O_{19}$ measured from BCDI. The dotted black rectangles depict zoomed-in regions where a type-I (antivortex-vortex) and type-II (antivortex-antivortex) Z_6 pairs are identified. **(D)** 2D slices of FE displacement normal to the BHF {107} atomic planes. The color bar range depicts antiphase domain displacements with opposite ferroelectrical polarization of magnitude 0.28 nm. The scale bars correspond to 100 nm.
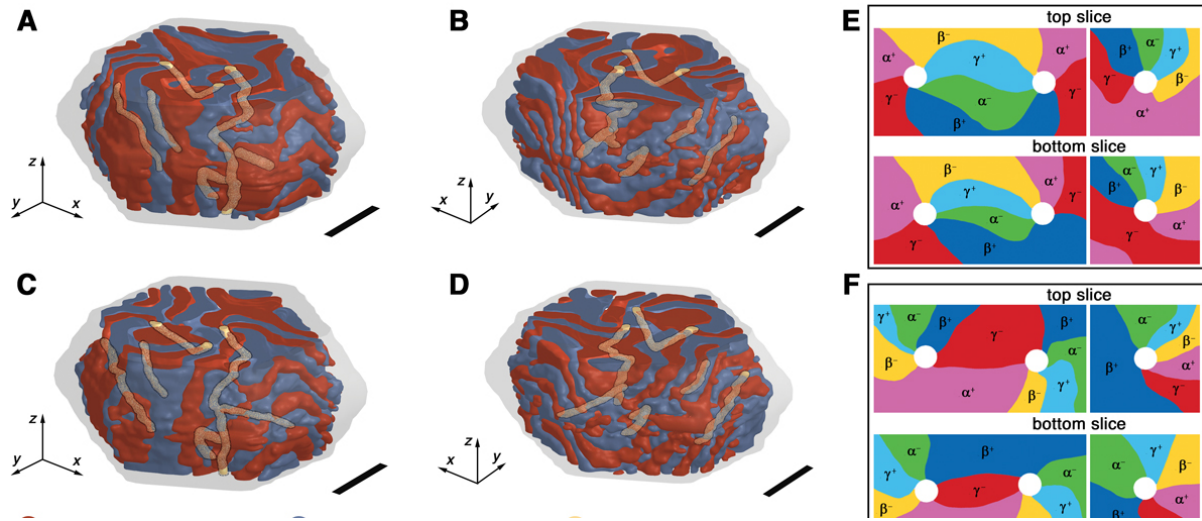
14

Figure 3. Volumetric evolution of 1D topological strings under applied electric field. (A) Front view showing 3D rendering of the reconstructed ferroelectric domains within a single BHF nanoparticle under zero electric field with vortex cores linked to form 1D topological strings. (**B**) Rear view of reconstructed BHF nanoparticle under zero electric field. (**C**) Front view of nanoparticle subjected to 10 V of applied field. (**D**) Rear view of the nanoparticle under 10 V. Schematic enlargements of the domain structures around vortex cores (white circles) for top and bottom planes identified with aid of Landau phase-field model at (**E**) 0 V and, (**F**) 10 V respectively. The vortices are topologically protected. Left panels of (**E**) and (**F**) show two vortices (vortex-antivortex pair) and right panels show a single antivortex. Scale bars correspond to 100 nm.
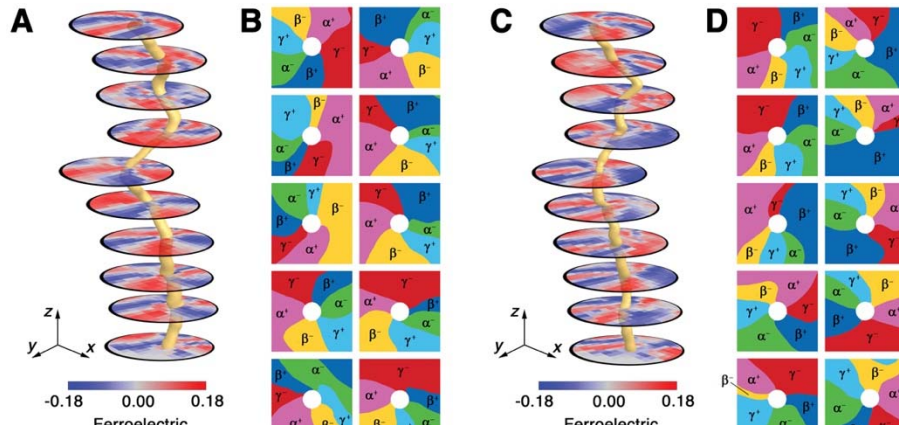
Figure 4. Evolution of the vorticity of electric polarization and depth profiling for 1D topological string. (A) The circular 2D cut planes show the evolution of the measured vorticity of ferroelectric polarization along 1D topological string when BHF is subjected to 0 V. **(B)** Schematic enlargement of the domain structures along the string in **(A)** with 6 phases identified with aid of a Landau model which provides better resolution than afforded by Bragg coherent diffractive imaging. **(C)** BCDI reconstructed vorticity under 10 V. **(D)** Schematic enlargements of the domain structures along the string in **(C)** with 6 phases identified with aid of the Landau model. The scale bars correspond to 40 nm.